APPROXIMATE INVERSE FOR THE COMMON OFFSET ACQUISITION GEOMETRY IN 2D SEISMIC IMAGING

CHRISTINE GRATHWOHL, PEER KUNSTMANN, ERIC TODD QUINTO,
AND ANDREAS RIEDER

Abstract. We explore how the concept of approximate inverse can be used and implemented to recover singularities in the sound speed from common offset measurements in two space dimensions. Numerical experiments demonstrate the performance of the method.

1. Introduction

In the inverse problem of seismology one seeks subsurface material parameters from measurements of reflected waves on a part of the propagation medium (typically an area on the earth's surface or in the ocean). To this end sources excite waves at certain positions and their reflections are recorded by receiver arrays. From a mathematical point of view we have to deal with a nonlinear parameter identification problem for a version of the elastic wave equation (with damping). This problem is solved by a multi-stage process which starts with determining the wave speed from a simpler model: the acoustic wave equation. By linearization (Born approximation) we are led to the generalized Radon transform (GRT) as a model for linear seismic imaging where the sound speed is averaged over reflection isochrones connecting sources and receivers (microphones) by points of equal travel time.

Let R be the GRT. Beylkin [2, 3] showed that there is a convolution type operator K and dual transform $R^\sharp$ (generalized backprojection operator) such that $\Psi = R^\sharp K R$ is a perturbation of the identity operator. Thus, from the measurement $g = Rf$ we can compute Ψf by applying $R^\sharp K$, i.e., $\Psi f = R^\sharp K g$. Classical GRT migration entails the direct application of K and $R^\sharp$ to the data g and is a state of the art reconstruction procedure in linearized seismology; see, for example, [36, Sec. 3] and [4, Chap. 5].

We advocate an alternative approach to this classical GRT migration scheme which we demonstrate in this paper for the common offset scanning geometry in two space dimensions and for a constant background velocity. In this situation the GRT becomes the elliptic Radon transform F which integrates over ellipses. We hasten to add that our approach is not bound to this simplified setting, see Remark 3.1 below for details.

As imaging operator we choose here $\Lambda = \Delta F^* \Phi F$ where Δ is the Laplacian, F^* is the formal adjoint in an L^2-space and Φ is a smooth cutoff function such that $F^*\Phi F$ is well defined. We argue that Λ is a pseudodifferential operator of order 1 and hence emphasizes some singularities by decreasing their Sobolev order by 1, see e.g. [28, Chap. 4.6], that is, Λf pronounces discontinuities of f in directions where Λ is microlocally elliptic. In

Date: June 26, 2018.

We gratefully acknowledge financial support by the Deutsche Forschungsgemeinschaft (DFG) through CRC 1173. Quinto additionally thanks the Otto Mønsteds Fond and U.S. National Science Foundation (under grants DMS 1311558 and DMS 1712207) for their support. He thanks colleagues at DTU and KIT for their warm hospitality while this research was being done.

this paper we propose a numerical scheme to recover Λf from the data (measurements) $g = \Phi F f$.

The structure of Λ is suited to apply the method of approximate inverse [24, 33] which has been successfully transferred to a variety of applications ranging from Doppler tomography [32], sonar [29], thermoacoustic tomography [19], inverse source problems for Maxwell's equation [23], local tomography [30], integral geometry [25] to atmospheric tomography [17]. This list is not complete by far.

Let $e_{\mathbf{p}}$ be a smooth approximation to the Dirac distribution concentrated about the reconstruction point $\mathbf{p} \in \mathbb{R}^{\mathbf{2}}$ and define $\psi_{\mathbf{p}} := F\Delta e_{\mathbf{p}}$. Then,

$$\langle g, \psi_{\mathbf{p}} \rangle = \langle \Phi F f, \psi_{\mathbf{p}} \rangle = \langle \Lambda f, e_{\mathbf{p}} \rangle \approx \Lambda f(\mathbf{p}),$$

i.e., the L^2-inner product of $\psi_{\mathbf{p}}$ with the data yields a stable approximation of the quantity we seek. Note that – in contrast to traditional Kirchhoff migration – the adjoint F^* is not needed explicitly. The evaluation of $\langle g, \psi_{\mathbf{p}} \rangle$ can be performed in parallel for different $\mathbf{p}$.

We should point out important work incorporating the GRT and microlocal analysis in seismic imaging. In [9], the GRT and a curvelet transform are used to reconstruct, and in [34], microlocal analysis is used in the presence of multipathing. The articles [8, 36] are good introductions with many further references.

In the following sections we motivate the selection of Λ, compute $\psi_{\mathbf{p}}$ semi-analytically for an explicitly given $e_{\mathbf{p}}$, and present numerical experiments to illustrate the performance of the scheme. For the sake of completeness and as a courtesy to the non-expert we derive the GRT from the acoustic wave equation in some detail. Our presentation in the next section is inspired by [5] and [35].

2. The imaging operator

2.1. **From the acoustic wave equation to the generalized Radon transform.** Let $u(t; \mathbf{x}, \mathbf{x_s})$ be the acoustic potential in $\mathbf{x} \in \mathbb{R}^2$ at time $t \geq 0$ satisfying the acoustic wave equation (with constant mass density)

$$\frac{1}{\nu^2}\, \partial_t^2 u - \Delta_{\mathbf{x}} u = \delta(\mathbf{x} - \mathbf{x_s})\delta(t) \tag{1}$$

where $\nu = \nu(\mathbf{x})$ is the speed of sound and $\mathbf{x_s}$ is the excitation (source) point. In seismic imaging one wants to recover ν from the backscattered (reflected) field $u(t; \mathbf{x_r}, \mathbf{x_s})$, $(t; \mathbf{x_r}, \mathbf{x_s}) \in Y := [0, T_{\max}] \times \mathcal{R} \times \mathcal{S}$ where $\mathcal{S}$ and $\mathcal{R}$ are the sets of source and receiver (microphone) positions, respectively, and $T_{\max}$ is the observation period.

We are making the ansatz

$$\frac{1}{\nu^2(\mathbf{x})} = \frac{1 + n(\mathbf{x})}{c^2(\mathbf{x})} \tag{2}$$

with a smooth and a priori known background velocity $c = c(\mathbf{x})$. Now, n is the quantity we seek. It is dimensionless and may physically be interpreted as a kind of reflectivity which captures the high frequency variations of ν, see, e.g., [4, Chap. 3.2.1]. As we present a rather formal derivation of a linear integral equation for determining n, see (6) below, we do not specify any assumptions on n for the time being, but we do in the next section. We follow the lines of [5] and [35].

Let $\widetilde{u}$ denote the solution of the above wave equation with sound speed c, i.e.,

$$\frac{1}{c^2}\, \partial_t^2 \widetilde{u} - \Delta_{\mathbf{x}} \widetilde{u} = \delta(\mathbf{x} - \mathbf{x_s})\delta(t). \tag{3}$$

We will use $\widetilde{u}$ to derive a linear equation for n.

Subtracting (1) from (3) and given (2) we find the equation

$$\frac{1}{c^2}\,\partial_t^2(\widetilde{u}-u)-\Delta_{\mathbf{x}}(\widetilde{u}-u)=\frac{n}{c^2}\,\partial_t^2 u$$

which is basically equivalent to the *Lippmann-Schwinger* integral equation, see, e.g., [6, Chap. 8.2].

Replacing u by $\widetilde{u}$ on the right of the above equation we perform the *Born approximation* to define the linear map

$$L\colon n\mapsto u_{\mathrm{d}}|_Y$$

where u_{d} solves

$$\frac{1}{c^2}\,\partial_t^2 u_{\mathrm{d}}-\Delta_{\mathbf{x}}u_{\mathrm{d}}=\frac{n}{c^2}\,\partial_t^2\widetilde{u}$$

and $Y=[0,T_{\max}]\times\mathcal{R}\times\mathcal{S}$. We may view L as a kind of linearization of the map $\mathcal{F}\colon\nu^2\mapsto u|_Y$, indeed, $\mathcal{F}(c^2)-\mathcal{F}(\nu^2)=\mathcal{F}(\nu^2+n\nu^2)-\mathcal{F}(\nu^2)\approx Ln$. The linearized problem for constant density seismic imaging now reads: Determine n from

$$Ln=\mathcal{F}(c^2)-\mathcal{F}(\nu^2)=\widetilde{u}|_Y-u|_Y$$

where $u|_Y$ has been recorded and $\widetilde{u}|_Y$ has to be computed from (3).

Using Duhamel's principle,

$$Ln(t;\mathbf{x_r},\mathbf{x_s})=\int\frac{n(\mathbf{x})}{c^2(\mathbf{x})}\Big(\int\partial_t^2\widetilde{u}(s;\mathbf{x},\mathbf{x_s})\widetilde{u}(t-s;\mathbf{x_r},\mathbf{x})\mathrm{d}s\Big)\mathrm{d}\mathbf{x}. \tag{4}$$

We now make the geometric optics approximation, that is, $\mathbf{x}\in\operatorname{supp}n$ can be connected to each $\mathbf{x_r}$ and to each $\mathbf{x_s}$ by one and only by one ray of geometric optics. Accordingly, $\widetilde{u}$ is a progressing wave in 2D:

$$\widetilde{u}(t;\mathbf{x},\mathbf{x_s})\approx a(\mathbf{x},\mathbf{x_s})\,\Psi\big(t-\tau(\mathbf{x},\mathbf{x_s})\big) \tag{5}$$

where

$$\Psi(t)=\frac{1}{2\pi}\begin{cases}t^{-1/2} & :\ t>0,\\ 0 & :\ t\le 0,\end{cases}$$

and where the travel time $\tau(\mathbf{x},\mathbf{x_s})$ solves the eikonal equation

$$|\nabla_{\mathbf{x}}\tau|=\frac{1}{c}$$

and the amplitude a satisfies

$$\operatorname{div}(a^2\nabla_{\mathbf{x}}\tau)=0,$$

see, e.g., Symes [35, pp. 24-25]. See also Friedlander [13] and Courant and Hilbert [7].

Remark 2.1. *The ansatz* (5) *is inspired by the fundamental solution E of the wave equation* (1) *with constant ν. For $\nu=1$ and $t\ge|\mathbf{x}-\mathbf{x_s}|$ we have that*

$$E(\mathbf{x},t)=\frac{1}{2\pi\sqrt{t^2-|\mathbf{x}-\mathbf{x_s}|^2}}=\frac{1}{\sqrt{t+|\mathbf{x}-\mathbf{x_s}|}}\,\Psi\big(t-|\mathbf{x}-\mathbf{x_s}|\big),$$

see, e.g., [26, Chap. 9.1].

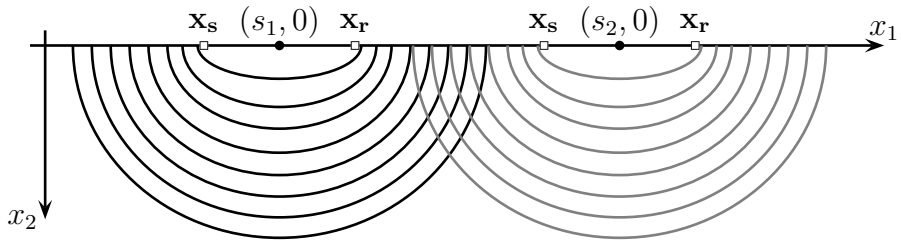

FIGURE 1. Common offset scanning geometry.

Plugging (5) into (4) we find that

$$\begin{aligned} Ln(t;\mathbf{x_r},\mathbf{x_s}) &\approx \partial_t^2 \int \frac{n(\mathbf{x})}{c^2(\mathbf{x})} a(\mathbf{x},\mathbf{x_s})a(\mathbf{x_r},\mathbf{x})\, \Psi \star \Psi\big(t-\tau(\mathbf{x},\mathbf{x_s})-\tau(\mathbf{x_r},\mathbf{x})\big)\,\mathrm{d}\mathbf{x} \\ &= \partial_t^2 \int \frac{n(\mathbf{x})}{4\pi\, c^2(\mathbf{x})} a(\mathbf{x},\mathbf{x_s})a(\mathbf{x_r},\mathbf{x}) H\big(t-\tau(\mathbf{x},\mathbf{x_s})-\tau(\mathbf{x_r},\mathbf{x})\big)\mathrm{d}\mathbf{x} \\ &= \partial_t \int \frac{n(\mathbf{x})}{4\pi\, c^2(\mathbf{x})} a(\mathbf{x},\mathbf{x_s})a(\mathbf{x_r},\mathbf{x}) \delta\big(t-\tau(\mathbf{x},\mathbf{x_s})-\tau(\mathbf{x},\mathbf{x_r})\big)\mathrm{d}\mathbf{x} =: \widetilde{L}n(t;\mathbf{x_r},\mathbf{x_s}) \end{aligned}$$

where the first equality holds since $\Psi \star \Psi = H/(4\pi)$ with H being the Heaviside function, see, e.g., [16, Chap. 1.5.5]. The second equality is true due to $H' = \delta$ where δ is the one-dimensional Dirac-distribution.

Set $u_{\mathrm{data}} := \widetilde{u} - u$. Our intermediate linear problem now reads

$$\widetilde{L}n(t;\mathbf{x_r},\mathbf{x_s}) = u_{\mathrm{data}}(t;\mathbf{x_r},\mathbf{x_s})$$

and integrating both sides with respect to t over the observation period from 0 to T we finally obtain

$$Fn(T;\mathbf{x_r},\mathbf{x_s}) = y(T;\mathbf{x_r},\mathbf{x_s}) \tag{6}$$

where

$$y(T;\mathbf{x_r},\mathbf{x_s}) := 4\pi \int_0^T u_{\mathrm{data}}(t;\mathbf{x_r},\mathbf{x_s})\mathrm{d}t$$

and

$$Fn(T;\mathbf{x_r},\mathbf{x_s}) = \int \frac{n(\mathbf{x})}{c^2(\mathbf{x})} a(\mathbf{x},\mathbf{x_s})a(\mathbf{x_r},\mathbf{x}) \delta\big(T-\tau(\mathbf{x},\mathbf{x_s})-\tau(\mathbf{x},\mathbf{x_r})\big)\mathrm{d}\mathbf{x} \tag{7}$$

is a generalized Radon transform which integrates over reflection isochrones $\{\mathbf{x} : T = \tau(\mathbf{x},\mathbf{x_s}) + \tau(\mathbf{x},\mathbf{x_r})\}$.

2.2. **The elliptic Radon transform.** In the following we assume that

- the background velocity c is constant, say, $c = 1$,
- $n \in L^2(\mathbb{R}^2_+)$ is compactly supported in $\mathbb{R}^2_+$ which is the lower half space $x_2 > 0$ (the positive direction of the x_2-axis points downwards to the interior of the earth),
- the common offset scanning geometry is used where source and receiver positions are located on the line $x_2 = 0$ and they are parameterized by $s \in \mathbb{R}$ via $(s-\alpha,0)^\top$ and $(s+\alpha,0)^\top$, respectively. Here, $\alpha > 0$ is the common offset.

Under these assumptions the reflection isochrones are ellipses with foci

$$\mathbf{x_s}(s) = (s-\alpha,0)^\top \quad \text{and} \quad \mathbf{x_r}(s) = (s+\alpha,0)^\top,$$

see Figure 1. Further,

$$\tau(\mathbf{x},\mathbf{y}) = |\mathbf{x}-\mathbf{y}| \quad \text{and} \quad a(\mathbf{x},\mathbf{y}) = \frac{1}{\sqrt{|\mathbf{x}-\mathbf{y}|}}.$$

In this situation the generalized Radon transform (7) integrates over ellipses and may be written as

$$Fn(s,t) = \int A(s,\mathbf{x})n(\mathbf{x})\delta\big(t-\varphi(s,\mathbf{x})\big)\mathrm{d}\mathbf{x}, \quad t > 2\alpha, \tag{8}$$

with

$$\varphi(s,\mathbf{x}) := |\mathbf{x_s}(s)-\mathbf{x}| + |\mathbf{x_r}(s)-\mathbf{x}| \quad \text{and} \quad A(s,x) = \frac{1}{\sqrt{|\mathbf{x_s}(s)-\mathbf{x}|\,|\mathbf{x_r}(s)-\mathbf{x}|}}.$$

The lower bound on t in (8) is needed because the major axis of the ellipse must be longer than half the distance between the foci.

2.3. **Local reconstruction operator and approximate inverse.** As we do not know an inversion formula for F we do not try to reconstruct n directly from its integrals $g = Fn$ over ellipses. Instead, we employ ideas from Lambda tomography [11] and define the reconstruction operator

$$\Lambda = \Delta F^* \Phi F$$

where $\Phi = \Phi(s,t)$ is a smooth compactly supported cutoff function, Δ is the Laplacian, and F^* is the *formal* L^2-adjoint of F satisfying

$$\langle F^* w, u\rangle_{L^2(\mathbb{R}^2)} = \langle w, Fu\rangle_{L^2(\mathbb{R}\times]2\alpha,\infty[)}.$$

Let us briefly explain our choice of Λ: under the Bolker assumption (see, e.g., [18, p. 371]), any hypersurface Radon transform R in an d-dimensional space and its (formal, smoothly weighted) L^2-adjoint R^* are Fourier integral operators of order $(1-d)/2$. Furthermore, if they can be composed, then R^*R is a pseudodifferential operator. Our transform F on $\mathbb{R}^2$ satisfies the Bolker assumption (this follows from [22, Theorem 4] which establishes the microlocal properties of this operator for functions supported on both sides of the axis $x_2 = 0$) so, $F^*\Phi F$ is of order -1 when Φ is a smooth cutoff function (which is needed so that F^* and F can be composed). Thus, Λ has order 1 and we expect

$$\Lambda n = \Delta F^* \Phi g$$

to emphasize singularities (e.g., jumps along curves) of n which are tangent to ellipses being integrated over (rigorously, covectors in the wavefront set of f that are normal to the ellipse which follows from [22, Theorem 3]). Further, Λ is local in the following sense: To reconstruct $\Lambda n(\mathbf{p})$ one only needs integrals over ellipses near to $\mathbf{p}$.

The structure of Λ is ideally suited to stabilize the evaluation of $\Lambda n(\mathbf{p})$ by the concept of approximate inverse, see [24]. Instead of $\Lambda n(\mathbf{p})$ we try to compute

$$\Lambda_\gamma n(\mathbf{p}) := \langle \Lambda n, e_{\mathbf{p},\gamma,k}\rangle_{L^2(\mathbb{R}^2)}$$

where

$$e_{\mathbf{p},\gamma,k}(\mathbf{x}) = C_{k,\gamma}\begin{cases}(\gamma^2-\Theta^2)^k & : \Theta < \gamma,\\ 0 & : \Theta \geq \gamma,\end{cases} \qquad \Theta = |\mathbf{x}-\mathbf{p}|,$$

with $\gamma, k > 0$ and

$$C_{k,\gamma} = \frac{k+1}{\pi\,\gamma^{2(k+1)}}.$$

We have $\operatorname{supp} e_{\mathbf{p},\gamma,k} = \overline{B_\gamma(\mathbf{p})}$, the closure of the ball about $\mathbf{p}$ with radius γ. Moreover, $\int e_{\mathbf{p},\gamma,k}(\mathbf{x})\mathrm{d}\mathbf{x} = 1$ such that $e_{\mathbf{p},\gamma,k} \to \delta(\cdot - \mathbf{p})$ as $\gamma \to 0$. Thus, γ serves as a scaling or

regularization parameter while k is a design parameter which determines the smoothness of $e_{\mathbf{p},\gamma,k}$. By its properties $e_{\mathbf{p},\gamma,k}$ is a mollifier.

Note that $\Lambda_\gamma n$ is well defined when $e_{\mathbf{p},\gamma,k} \in H_0^1(\mathbb{R}^2)$ ($k \geq 1$ is sufficient). Indeed, by our assumption on n we have that $\Lambda n \in H^{-1}_{\mathrm{loc}}(\mathbb{R}^2_+)$, see, e.g., [28, Theorem 4:5.12].

Lemma 2.2. *Let $k \geq 3$. Under the assumptions of Section 2.2 we have that*

$$\Lambda_\gamma n(\mathbf{p}) = \langle \Phi F n, \psi_{\mathbf{p},\gamma,k} \rangle_{L^2(\mathbb{R}\times]2\alpha,\infty[)}$$

with

$$\psi_{\mathbf{p},\gamma,k}(s,t) = 4k\, C_{k,\gamma}\Big((k-1)\, F\big(|\cdot - \mathbf{p}|^2\, \widetilde{e}_{\mathbf{p},\gamma,k-2}\big)(s,t) - F\widetilde{e}_{\mathbf{p},\gamma,k-1}(s,t)\Big) \tag{9}$$

where $\widetilde{e}_{\mathbf{p},\gamma,k} = e_{\mathbf{p},\gamma,k}/C_{k,\gamma}$. Moreover, the following translation invariance holds

$$\psi_{\mathbf{p},\gamma,k}(s,t) = \psi_{(0,p_2),\gamma,k}(s-p_1,t).$$

Proof. By duality

$$\Lambda_\gamma n(\mathbf{p}) = \langle \Delta F^* \Phi F n, e_{\mathbf{p},\gamma,k} \rangle = \langle \Phi F n, \psi_{\mathbf{p},\gamma,k} \rangle$$

with

$$\psi_{\mathbf{p},\gamma,k} = F\Delta e_{\mathbf{p},\gamma,k} = C_{k,\gamma} F \Delta \widetilde{e}_{\mathbf{p},\gamma,k}$$

and $\Delta\widetilde{e}_{\mathbf{p},\gamma,k} = 4k(k-1)\,|\cdot - \mathbf{p}|^2\, \widetilde{e}_{\mathbf{p},\gamma,k-2} - 4k\, \widetilde{e}_{\mathbf{p},\gamma,k-1}$ yields (9).

The translation invariance is a direct consequence of the translation invariances of the Laplacian and of F with respect to s: $Fn(s-r,t) = F\big(n(\cdot - r,\cdot)\big)(s,t)$. □

Lemma 2.2 tells us that we can compute $\Lambda_\gamma n(\mathbf{p})$ from the data g if we can evaluate the function $\psi_{\mathbf{p},\gamma,k}$ which is called a reconstruction kernel for F (belonging to the mollifier $e_{\mathbf{p},\gamma,k}$). The translation invariance of the reconstruction kernel might be used to speed up the computation of $\Lambda_\gamma n(\mathbf{p})$ as one only needs to evaluate $\psi_{(0,p_2),\gamma,k}$ numerically.

Note that we do not need to know F^* explicitly to compute $\Lambda_\gamma n(\mathbf{p})$.

3. Computing the reconstruction kernel

Calculating the reconstruction kernel $\psi_{\mathbf{p},\gamma,k}$ according to (9) requires the application of our imaging operator F, see (8), to functions which are supported in a ball. In a first step we therefore present an explicit calculation of F acting on the indicator function of a ball. This will be used for the general case, which is discussed at the end of this section.

Let χ be the indicator function of $B_r(\mathbf{p})$ with $p_2 > 0$, and radius r where $0 < r < p_2$, that is, $B_r(\mathbf{p})$ is completely contained in the lower half space (recall that the positive x_2-direction points downwards). We are going to recast

$$F\chi(s,t) = \int A(s,\mathbf{x})\chi(\mathbf{x})\delta\big(t - \varphi(s,\mathbf{x})\big)\mathrm{d}\mathbf{x}, \quad t > 2\alpha,$$

as an integral explicitely along isochrons. The advantage of integrating along isochrons for seismic inversion has been known for some time, see, e.g., [37].

Using prolate spheroidal coordinates depending on $(s,0)^\top$ given by

$$\mathbf{x}(s,t,\phi) = (x_1,x_2)^\top \tag{10}$$

where

$$x_1 = s + \frac{t}{2}\cos\phi, \quad \text{and} \quad x_2 = \sqrt{\frac{t^2}{4} - \alpha^2}\ \sin\phi,$$

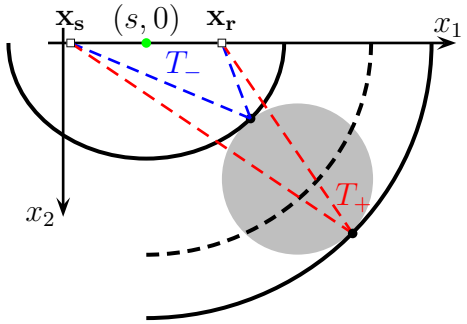

FIGURE 2. Geometric illustration of the definition of T_- and T_+. The light gray disk is the support of χ.

we find from our calculations in Appendix A that

$$F\chi(s,t) = \int_0^\pi A\big(s,\mathbf{x}(s,t,\phi)\big)\chi\big(\mathbf{x}(s,t,\phi)\big)\,\frac{t^2/4-\alpha^2\cos^2\phi}{\sqrt{t^2-4\alpha^2}}\,\mathrm{d}\phi.$$

As

$$A\big(s,\mathbf{x}(s,\varrho,\phi)\big) = \frac{1}{\sqrt{|\mathbf{x_s}(s)-\mathbf{x}|\,|\mathbf{x_r}(s)-\mathbf{x}|}} = \frac{1}{\sqrt{t^2/4-\alpha^2\cos^2\phi}}$$

we obtain

$$F\chi(s,t) = \int_0^\pi \chi\big(\mathbf{x}(s,t,\phi)\big)\,\frac{\sqrt{t^2/4-\alpha^2\cos^2\phi}}{\sqrt{t^2-4\alpha^2}}\,\mathrm{d}\phi. \tag{11}$$

Note that we can restrict the integration over ϕ to the interval $[0,\pi]$ because χ is supported in the lower half space where $x_2 = \sqrt{t^2/4-\alpha^2}\,\sin\phi$ is non-negative.

To evaluate $F\chi(s,t)$ further we provide the following quantities

$$T_- = T_-(s,r,\mathbf{p}) = \min\big\{\varphi(s,\mathbf{x}) : \mathbf{x}\in\partial B_r(\mathbf{p})\big\},$$
$$T_+ = T_+(s,r,\mathbf{p}) = \max\big\{\varphi(s,\mathbf{x}) : \mathbf{x}\in\partial B_r(\mathbf{p})\big\}.$$

Let $E(s,t)$ be the ellipse with foci $\mathbf{x_s}(s)$, $\mathbf{x_r}(s)$ and travel time (major diameter) $t>2\alpha$. Then,

$$E(s,t)\cap B_r(\mathbf{p})\neq\emptyset \quad \text{if and only if} \quad T_- < t < T_+$$

which is a direct consequence of the definition of $T_\pm$, see Figure 2 for a geometric illustration. From that we get

$$F\chi(s,t) = \begin{cases} 0 & : \ t\notin\,]T_-,T_+[, \\ \displaystyle\int_{\phi_1}^{\phi_2} \frac{\sqrt{t^2/4-\alpha^2\cos^2\phi}}{\sqrt{t^2-4\alpha^2}}\,\mathrm{d}\phi & : \ t\in\,]T_-,T_+[, \end{cases} \tag{12}$$

where

$$\phi_1 = \phi_1(s,t) = \min\big\{\phi : \mathbf{x}(s,t,\phi)\in\overline{B_r(\mathbf{p})}\,\big\},$$
$$\phi_2 = \phi_2(s,t) = \max\big\{\phi : \mathbf{x}(s,t,\phi)\in\overline{B_r(\mathbf{p})}\,\big\}.$$

So it remains to find numerical approximations for T_-, T_+, and ϕ_1, ϕ_2. For the first pair of values we parameterize $\partial B_r(\mathbf{p})$ by

$$\partial B_r(\mathbf{p}) = \big\{\mathbf{p}+r(\cos\vartheta,\sin\vartheta)^\top : \vartheta\in[0,2\pi[\,\big\},$$

so that

$$T_{-/+} = \min / \max \left\{ \widetilde{\varphi}(\vartheta) : \vartheta \in [0, 2\pi[\right\} \quad \text{where} \quad \widetilde{\varphi}(\vartheta) := \varphi\big(s, \mathbf{p} + r(\cos\vartheta, \sin\vartheta)^\top\big).$$

From the geometric setting it becomes evident that $\widetilde{\varphi}$ attains exactly one minimum and one maximum in $[0, 2\pi[$. As both extrema are clearly separated, we can apply Newton's method to get the two zeros of $\widetilde{\varphi}'$.

Having $T_\mp$ we solve

$$r^2 = |\mathbf{p} - \mathbf{x}(s, t, \phi)|^2$$

for ϕ. Given $t \in]T_-, T_+[$ and $s \in \mathbb{R}$ we have exactly the two solutions ϕ_1 and ϕ_2. Plugging in prolate spheroidal coordinates we get the equation

$$r^2 = (p_1 - s)^2 + p_2^2 + \frac{t^2}{4} - \alpha^2 - \sqrt{t^2 - 4\alpha^2}\, p_2 \sin\phi - (p_1 - s)\, t \cos\phi + \alpha^2 \cos^2\phi.$$

We substitute

$$\begin{aligned} z &= \cos\phi, \\ b &= -(p_1 - s)\, t, \\ c &= (p_1 - s)^2 + p_2^2 + \frac{t^2}{4} - \alpha^2 - r^2, \\ d &= -\sqrt{t^2 - 4\alpha^2}\, p_2, \end{aligned}$$

to obtain the equation

$$-d\sqrt{1 - z^2} = c + b\, z + \alpha^2\, z^2$$

for z which has exactly two solutions in $[-1, 1]$. Using Newton's method again we compute the two solutions $z_2 < z_1$ in $[-1, 1]$ and get

$$\phi_i = \arccos z_i, \quad i = 1, 2.$$

Having found these angles, we can calculate a numerical value for $F\chi(s, t)$, see (12). Please note that, for $t \in]T_-, T_+[$, $F\chi(s, t)$ represents an incomplete elliptic integral of the second kind which cannot be written in terms of elementary functions but implementations in most programming languages are available.

The reconstruction kernel $\psi_{\mathbf{p},\gamma,k}$ can be computed numerically in the same way as $F\chi$. Indeed, for, $t \in]T_-, T_+[$,

$$\psi_{\mathbf{p},\gamma,k}(s, t) = F\Delta e_{\mathbf{p},\gamma,k}(s, t) = \int_{\phi_1}^{\phi_2} \Delta e_{\mathbf{p},\gamma,k}\big(\mathbf{x}(s, t, \phi)\big)\, \frac{\sqrt{t^2/4 - \alpha^2\cos^2\phi}}{\sqrt{t^2 - 4\alpha^2}}\, \mathrm{d}\phi.$$

To simplify the kernel calculation we use that

$$\begin{aligned} \frac{\sqrt{t^2/4 - \alpha^2\cos^2\phi}}{\sqrt{t^2 - 4\alpha^2}} &= \frac{1}{2}\, \frac{\sqrt{t^2 - 4\alpha^2\cos^2\phi}}{\sqrt{t^2 - 4\alpha^2}} \\ &= \frac{1}{2} + (1 - \cos^2\phi)\frac{\alpha^2}{t^2} + \mathrm{O}(\tfrac{\alpha^4}{t^4}) \approx \frac{1}{2} \quad \text{for } t \gg \alpha \end{aligned}$$

and define an approximate kernel $\widetilde{\psi}_{\mathbf{p},\gamma,k}$ via

$$\widetilde{\psi}_{\mathbf{p},\gamma,k}(s, t) := F_{\text{approx}}\Delta e_{\mathbf{p},\gamma,k}(s, t) := \frac{1}{2}\int_{\phi_1}^{\phi_2} \Delta e_{\mathbf{p},\gamma,k}\big(\mathbf{x}(s, t, \phi)\big)\, \mathrm{d}\phi. \tag{13}$$

For instance, let $k = 3$. Then,

$$\Delta e_{\mathbf{p},\gamma,3}(\mathbf{x}) = C_{3,\gamma}\big(-36\,|\mathbf{x} - \mathbf{p}|^4 + 48\gamma^2\,|\mathbf{x} - \mathbf{p}|^2 - 12\gamma^4\big)\chi_{B_\gamma(\mathbf{p})}(\mathbf{x}).$$

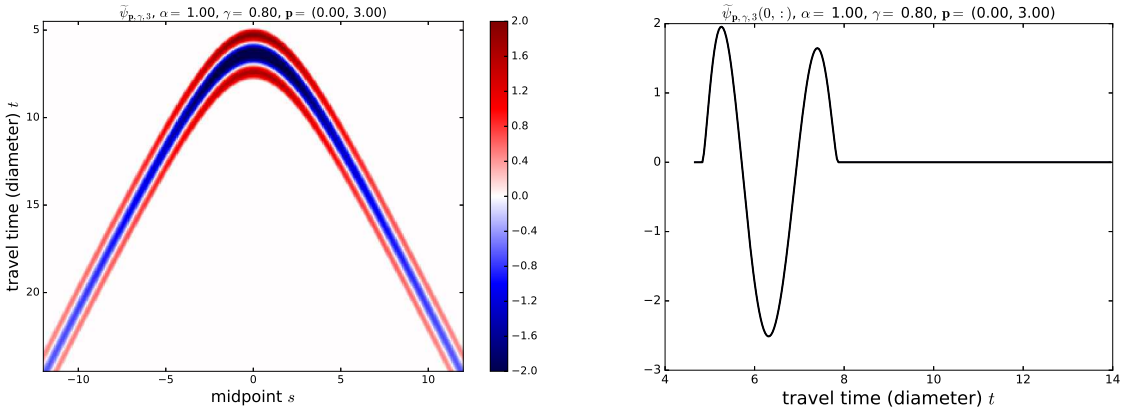

FIGURE 3. Reconstruction kernel $\widetilde{\psi}_{\mathbf{p},\gamma,3}$ (13) for $\gamma = 0.8$ and $\alpha = 1$ at $\mathbf{p} = (0, 3)$. The cross section on the right is taken for $s = 0$.

Now F_{approx} can be applied to each of the components of $\Delta e_{\mathbf{p},\gamma,3}$. Consider

$$F_{\text{approx}}\big(|\cdot - \mathbf{p}|^4 \chi_{B_\gamma(\mathbf{p})}\big)(s,t) = \begin{cases} 0 & : \ t \notin]T_-, T_+[, \\ \dfrac{1}{2}\displaystyle\int_{\phi_1}^{\phi_2} |\mathbf{x}(s,t,\phi) - \mathbf{p}|^4 \, \mathrm{d}\phi & : \ t \in]T_-, T_+[. \end{cases}$$

Here,

$$|\mathbf{x}(s,t,\phi) - \mathbf{p}|^4 = \left(\left(s - p_1 + \frac{t}{2}\cos\phi \right)^2 + \left(\sqrt{\frac{t^2}{4} - \alpha^2}\ \sin\phi - p_2 \right)^2 \right)^2$$

is a trigonometric polynomial in ϕ whose antiderivative is known analytically, that is, we have an explicit expression for $\widetilde{\psi}_{\mathbf{p},\gamma,3}(s,t)$ in terms of the trigonometric functions and of T_-, T_+, and ϕ_1, ϕ_2. See Figure 3 for a graphical example. From its definition (13) it becomes clear that the kernel resembles the reflection response of a point reflector.

Remark 3.1. *In this remark we discuss assumptions, limitations and generalizations of our approach.*

We rely crucially on the single-ray assumption to derive the linearized equation (6) *with some mathematical rigor. But it has been observed in the literature that the linear model* (6) *works well for more general background wave speeds, see, e.g.,* [4, pages 102 and 238].

Our migration/reconstruction technique can cope, in principal, with non-constant background wave speed: When F is the GRT (7) *the imaging operator Λ and the reconstruction kernel $\psi_{\mathbf{p},\gamma} := F\Delta e_{\mathbf{p},\gamma}$ remain well defined. To evaluate the kernel we have to solve numerically the eikonal equation as well the transport equation using ray tracing techniques, see, e.g.,* [4, Appendix E]. *Further, scanning geometries other than common offset can be dealt with, see the remark about other acquisition geometries in the next section.*

In future research we will consider more general imaging operators of the type

$$\Lambda = P^* F^* \Phi F$$

where P^* is the dual of a local operator such that Λ is of order 1 to emphasize singularities. We will compute and study the symbol of Λ to find useful P's and corresponding reconstruction kernels.

Finally, we would like to comment on other recent work to linearize seismic inversion without using the single-ray assumption explicitly. As a representative we consider [9]*. Here, the linearized operator F is derived differently, namely as a formal Fréchet derivative of the solution of the wave equation with respect to wave speed and mass density. Now, the authors argue that F is a zero-th order FIO with a canonical graph (under some assumptions). They show further that F^*F admits a sparse matrix approximation in a curvelet system. An implementation of this approach is demanding. It requires the careful evaluation of oscillatory integrals whose phase functions have to be determined from a set of partial differential equations related to the graph. In principle, all these challenges can be mastered, however, we are not aware of an implementation using this or a similar approach, but see* [1] *for a curvelet code for reverse time migration.*

4. Numerical experiments

We want to compute numerical approximations to

$$\Lambda_\gamma n(\mathbf{p}) := \langle \Lambda n, e_{\mathbf{p},\gamma,3}\rangle_{L^2(\mathbb{R}^2)} = \langle \Phi F n, \psi_{\mathbf{p},\gamma,3}\rangle_{L^2(\mathbb{R}\times]2\alpha,\infty[)} \tag{14}$$

from the discrete data

$$g(i,j) = \Phi(s_i,t_j)Fn(s_i,t_j), \quad i=1,\dots,N_s,\ j=1,\dots,N_t, \tag{15}$$

where

$$\{s_i\} \subset [-s_{\max}, s_{\max}] \quad \text{and} \quad \{t_j\} \subset [t_{\min}, t_{\max}],\ t_{\min} > 2\alpha,$$

are uniformly distributed with step sizes h_s and h_t, respectively. By a simple approximation of the double integral on the right of (14) and using the approximate kernel $\widetilde{\psi}_{\mathbf{p},\gamma,3}$ (13) we get

$$\begin{aligned}\Lambda_\gamma n(\mathbf{p}) \approx \widetilde{\Lambda}_\gamma n(\mathbf{p}) &:= h_s h_t \sum_{i=1}^{N_s}\sum_{j=1}^{N_t} g(i,j)\,\widetilde{\psi}_{\mathbf{p},\gamma,3}(s_i,t_j) \\ &= h_s h_t \sum_{i=1}^{N_s}\sum_{t_j\in\mathcal{T}_i(\mathbf{p})} g(i,j)\,\widetilde{\psi}_{\mathbf{p},\gamma,3}(s_i,t_j)\end{aligned} \tag{16}$$

with $\mathcal{T}_i(\mathbf{p}) = \left]T_-(s_i,\gamma,\mathbf{p}), T_+(s_i,\gamma,\mathbf{p})\right[$.

Remark 4.1. *A comment on the selection of the scaling/regularization parameter γ is appropriate here. A general and meaningful strategy, which works in practical situations, seems to be missing in the theory of the approximate inverse, but see* [31] *for an asymptotic result in an abstract setting.*

As a regularization parameter, γ depends on the discretization step size, number of measurements, and noise level. However, the proper interaction of these quantities is subtle. We will derive a rough guess around which a useful γ may be found empirically. Our working hypothesis is: γ should be such that the kernel is well resolved by its discrete samples $\{\widetilde{\psi}_{\mathbf{p},\gamma,3}(s_i,t_j)\}$. Let $\alpha = 0$, fix s_i and consider the cross section $\widetilde{\psi}_{\mathbf{p},\gamma,3}(s_i,\cdot)$ which is supported in $\mathcal{T}_i(\mathbf{p})$ and oscillates there. With a view on Figure 3 *we see that* 3 *samples in this interval are sufficient:*

$$|\mathcal{T}_i(\mathbf{p})| \geq 3h_t.$$

Further, $|\mathcal{T}_i(\mathbf{p})| = 4\gamma$ since $\alpha = 0$. Hence, $\gamma \geq 3h_t/4$. However, we also have to resolve the oscillations in the s-direction. The support of $\widetilde{\psi}_{\mathbf{p},\gamma,3}(\cdot,t_j)$ splits into two intervals

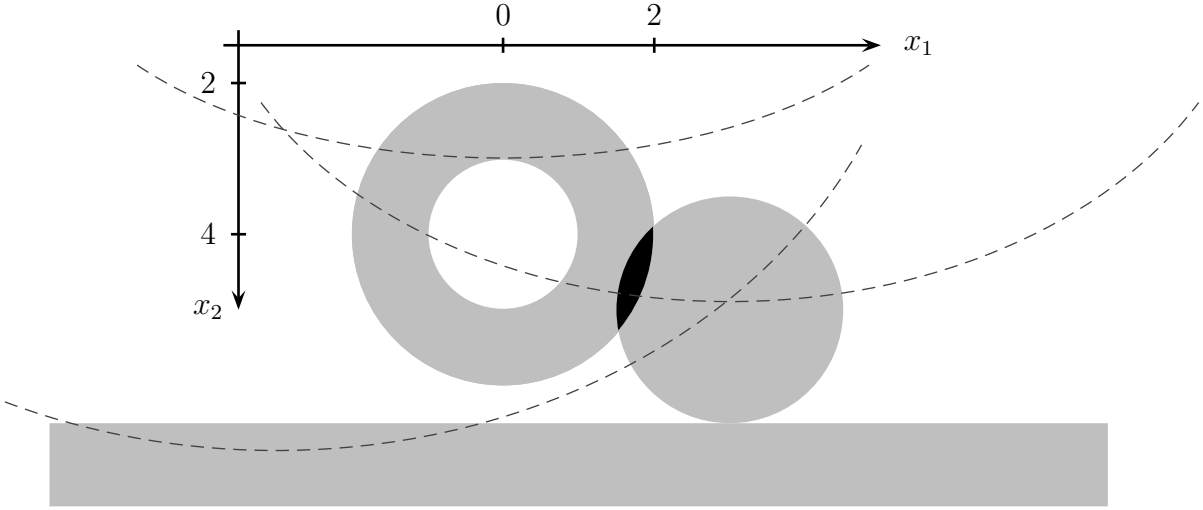

FIGURE 4. Visualization of the function n (17) to be reconstructed from elliptic means. Light gray area: $n = 1$, black: $n = 2$, white: $n = 0$. The light gray bar represents the half space $x_2 \geq 6.5$. The three dashed curves show elliptic arcs belonging to the common offset $\alpha = 5$ and $s = 0$, $t = 12$ (top), $s = 3$, $t = 14$ (middle), $s = -3$, $t = 17$ (bottom).

for t_j large enough, compare Figure 3. *Each of these intervals is larger than 2γ but approaching this value as t_j increases. Again, with* 3 *samples we resolve the oscillations in these intervals: $2\gamma \geq 3h_s$. Thus, we suggest to choose*

$$\gamma = C_{\alpha,\varepsilon}\,\frac{3}{2}\max\{h_t/2, h_s\}$$

where $C_{0,0} \approx 1$ and where $C_{\alpha,\varepsilon}$ needs to be gradually increased with α and ε. The quantity ε represents the magnitude of measurement noise in the data, see (18) *and Figure* 9 *below.*

For a first numerical experiment the function to be reconstructed is

$$n = \chi_{B((0,4),2)} - \chi_{B((0,4),1)} + \chi_{B((3,5),1.5)} + \chi_{x_2 \geq 6.5}, \tag{17}$$

see Figure 4. The data $g = \Phi F n$ for the common offset $\alpha = 5$ are plotted in Figure 5. They have been computed semi-analytically using (12). Observe the effect of the cutoff function Φ at the edges. We used the design of $\Phi \in \mathcal{C}^\infty(\mathbb{R}^2)$ from [29, Sec. 5]: Given $0 < \eta < \overline{T}$ and $\overline{S} > 0$ we define

$$\Phi(s,t) = \Phi_1(s)\Phi_2(t)$$

where

$$\Phi_2(t) = \begin{cases} 0 & : t \leq \eta \text{ or } t \geq \overline{T} + 1, \\ 1 & : \quad 2\eta \leq t \leq \overline{T}, \\ p(t,\overline{T}) & : \quad \overline{T} < t < \overline{T} + 1, \\ q(t,\eta) & : \quad \eta < t < 2\eta, \end{cases}$$

with

$$p(t,\overline{T}) = \frac{u(\overline{T} + 1 - t)}{u(\overline{T} + 1 - t) + u(t - \overline{T} - 1/2)}, \quad q(t,\eta) = \frac{u(t/\eta - 1)}{u(t/\eta - 1) + u(2 - t/\eta)},$$

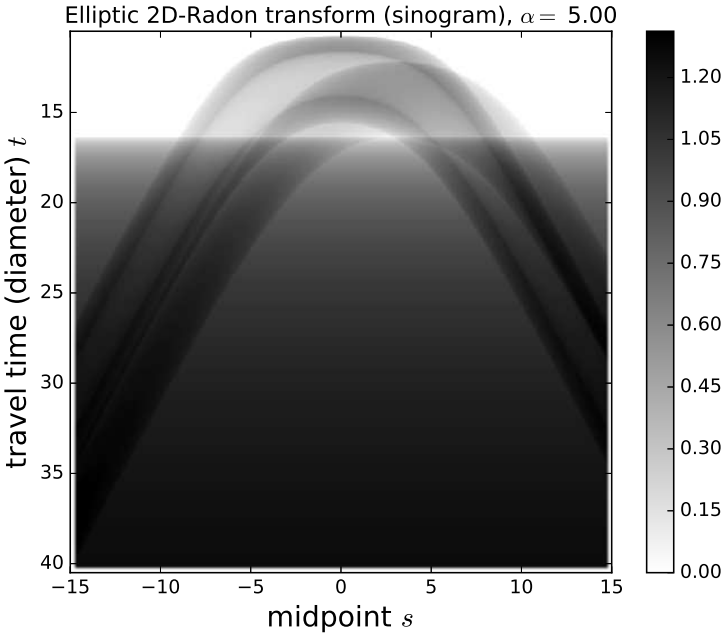

FIGURE 5. Elliptic Radon transform ΦFn for n from (17) and F from (11) with common offset $\alpha = 5$. The numerical values for $\Phi Fn(s,t)$ have been computed semi-analytically using (12).

and

$$u(r) = \begin{cases} \exp(-1/r) & : r > 0, \\ 0 & : r \leq 0. \end{cases}$$

Further,

$$\Phi_1(s) = \begin{cases} 1 & : \quad |s| < \overline{S}, \\ p(|s|, \overline{S}) & : \overline{S} \leq |s| \leq \overline{S} + 1, \\ 0 & : \quad |s| > \overline{S} + 1. \end{cases}$$

Thus,

$$\operatorname{supp} \Phi \subset [-s_{\max}, s_{\max}] \times [0.01, t_{\max}] \quad \text{and} \quad \Phi|_{[-s_{\max}+1, s_{\max}-1] \times [0.02, t_{\max}-1]} = 1$$

with our choice $\overline{T} := t_{\max} - 1$, $\eta := 0.01$, and $\overline{S} = s_{\max} - 1$.

For the computation of $\widetilde{\Lambda}_\gamma n$ we used $s_{\max} = 15$, $t_{\max} = t_{\min} + 30$ with $t_{\min} = 5$ for $\alpha = 2$ and $t_{\min} = 10.5$ for $\alpha = 5$. All reconstructions have been computed from $N_s\, N_t = 600^2 = 360000$ elliptic means.

We approximated $\widetilde{\Lambda}_\gamma n(\mathbf{p})$ for $\mathbf{p}$ uniformly in $[-2.5, 5] \times [1.5, 7]$ using 150 equidistant points for each interval. The results for the scaling $\gamma = 0.2$ are shown in Figure 6. Restricting the data set reduces the visible singularities in the reconstruction: Figure 7 displays a reconstruction where $s_{\max} = 7.5$ and $t_{\max} = 25.50$. Compared to the bottom reconstruction of Figure 6 those singularities are missing whose tangents have a dominant vertical component: This data set does not include integrals over ellipses tangent to those singularities.

As F^* and F cannot be meaningfully composed we introduced the smooth cutoff function Φ in the definition of Λ. However, in our numerical experiments we can easily get rid of Φ by setting $\Phi(s_i, t_j) = 1$ in (15) for all i and j. Figure 8 displays the difference of such

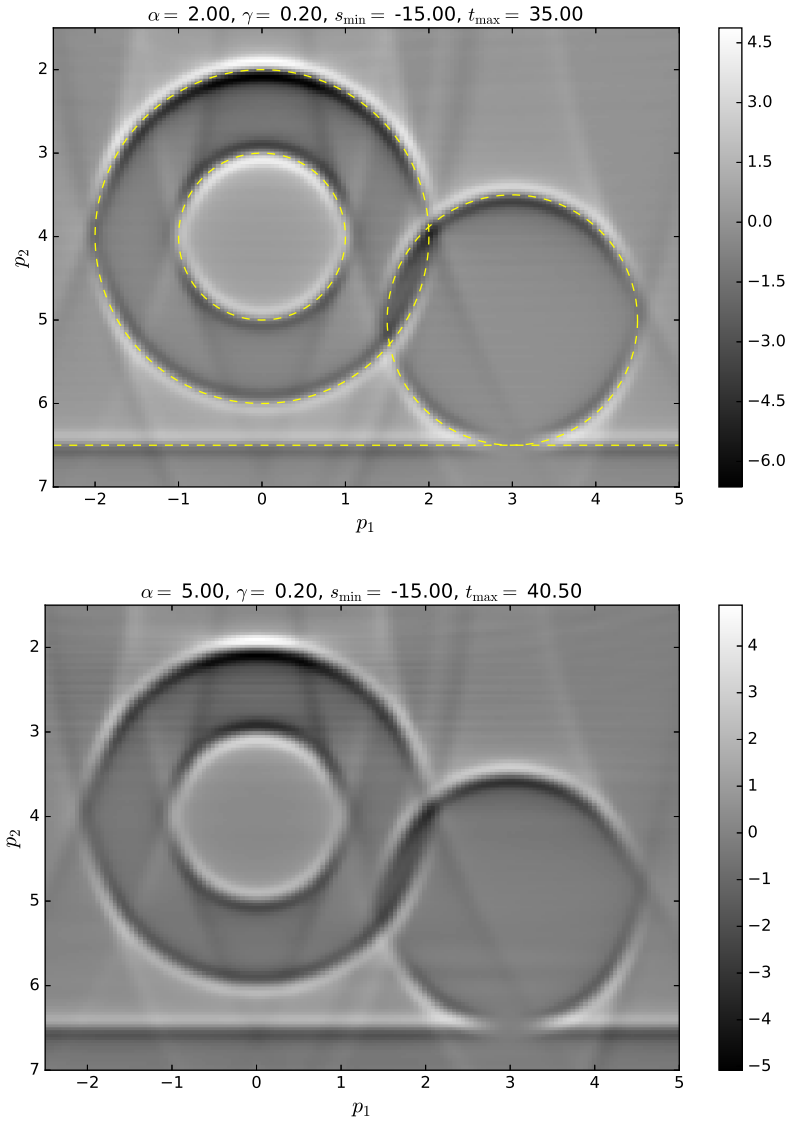

FIGURE 6. Reconstructions $\widetilde{\Lambda}_\gamma n$, $\gamma = 0.2$, with n from (17). Top: common offset $\alpha = 2$, bottom: common offset $\alpha = 5$. Further, $N_s = N_t = 600$. The dashed lines in the top image indicate the singular support of n and are not part of the reconstruction.

a reconstruction without a cutoff and the corresponding reconstruction with a smooth cutoff (which is the reconstruction from the bottom of Figure 6). We see that both reconstructions capture the singularities of n consistently: their difference does not contain a trace of these singularities. On the other hand, the reconstructions differ greatly in the added, unphysical singularities which are caused by the limited data and the numerical scheme. Introducing the cutoff function damps significantly the intensity of the artificial singularities termed 'endpoint artifacts' in [4, Chap. 5.7]. This is a general phenomenon that has been analyzed for tomography problems including limited angle X-ray CT [21, 14, 27], sonar, and photoacoustic tomography [15].

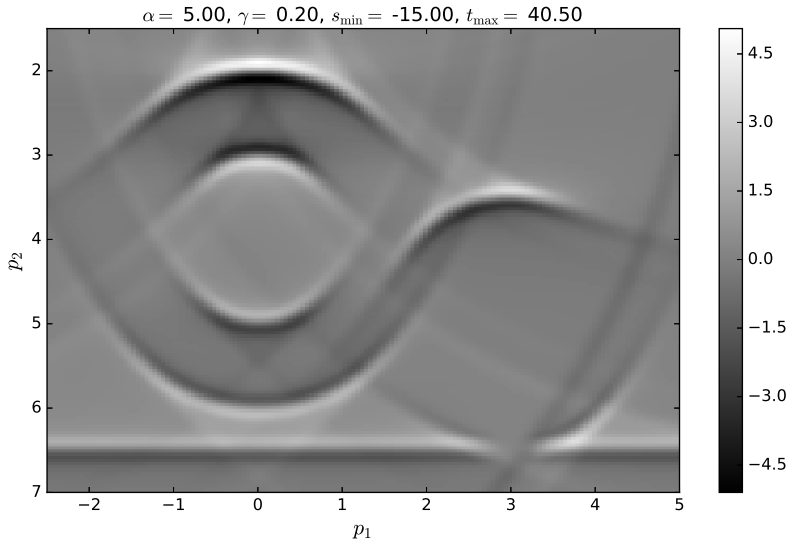

FIGURE 7. Reconstruction $\widetilde{\Lambda}_\gamma n$, $\gamma = 0.2$, with n from (17). The common offset is $\alpha = 5$. The other used parameters are $s_{\max} = 7.5$, $t_{\max} = 25.50$, $N_s = N_t = 600$.

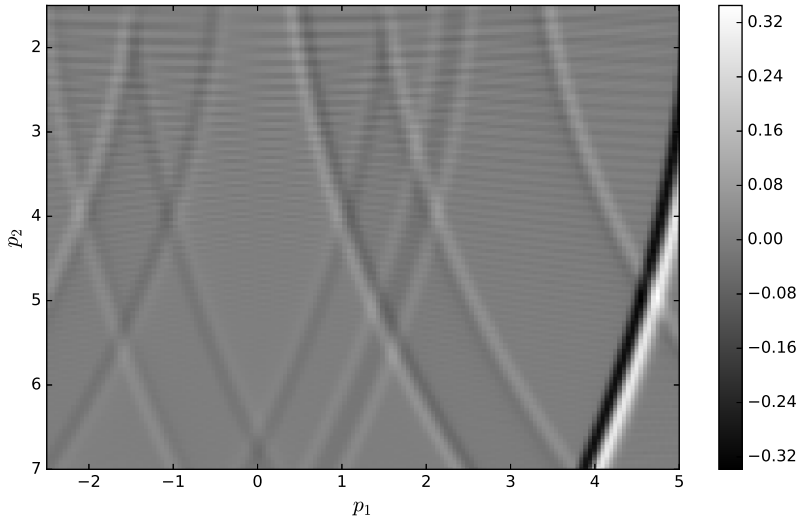

FIGURE 8. Difference of a reconstruction without the smooth cutoff function Φ and of a reconstruction with Φ.

Next, we demonstrate how $\widetilde{\Lambda}_\gamma n$ is affected by perturbed data which we generated according to

$$g^\varepsilon(i,j) = g(i,j) + \varepsilon \, \|g\|_\star \, \frac{\mathtt{n}(i,j)}{\|\mathtt{n}\|_\star}, \quad \varepsilon > 0, \tag{18}$$

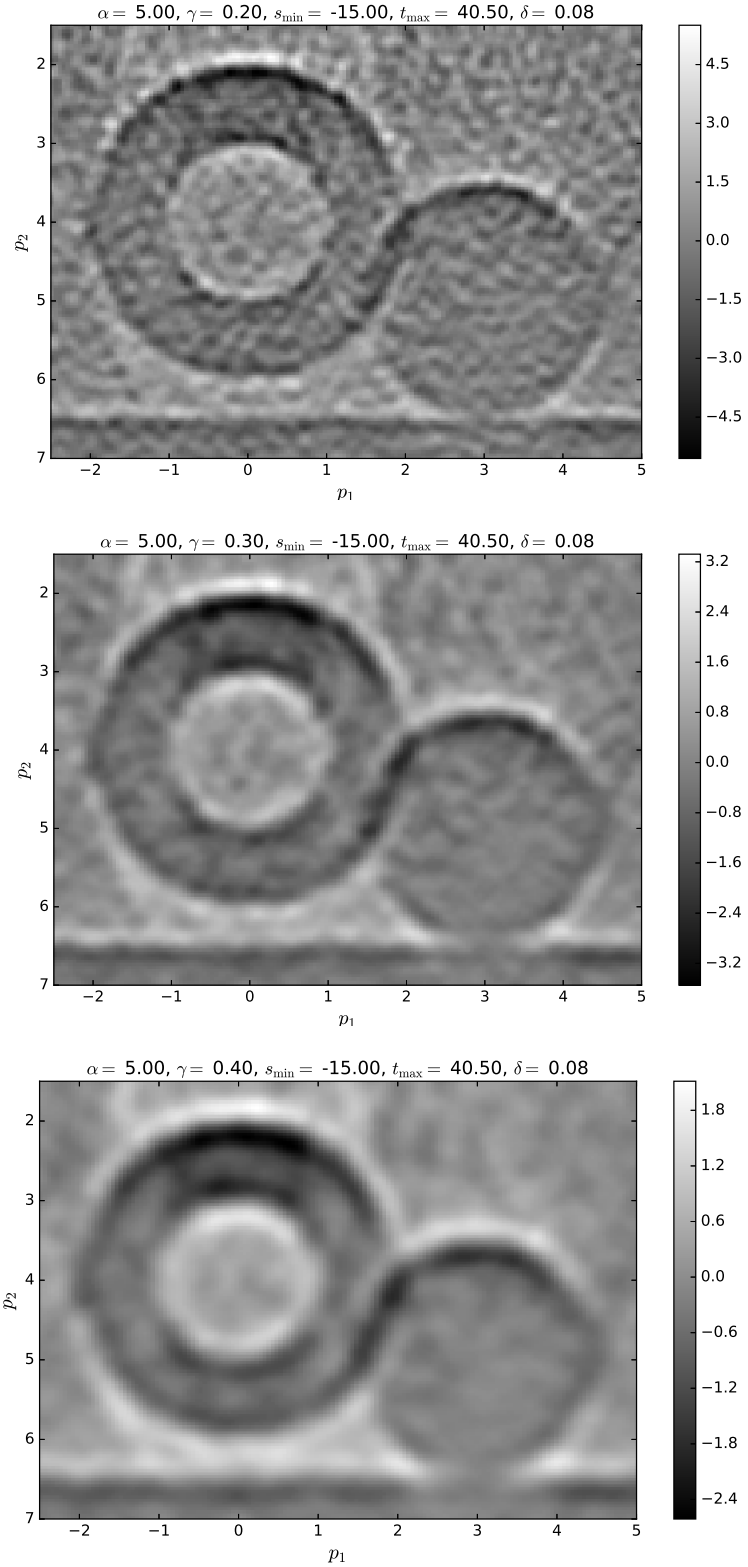

FIGURE 9. Reconstructions $\widetilde{\Lambda}_\gamma n$ from the same perturbed data set with $\varepsilon = 8\%$, see (18). Top: $\gamma = 0.2$, middle: $\gamma = 0.3$, bottom: $\gamma = 0.4$. All other parameters are as in Figure 6.

where g is the exact data (15) and $\mathtt{n}$ is an $N_s \times N_t$ array of uniformly distributed random numbers with values in $[-1, 1]$. The discrete norm

$$\|g\|_\star^2 := h_s h_s \sum_{i=1}^{N_s} \sum_{j=1}^{N_t} |g(i,j)|^2$$

approximates the norm in $L^2\big([-s_{\max}, s_{\max}] \times [t_{\min}, t_{\max}]\big)$. We have that

$$\frac{\|g - g^\varepsilon\|_\star}{\|g\|_\star} \leq \varepsilon,$$

i.e., ε measures the *relative noise*. Figure 9 shows reconstructions for a data set with noise level $\varepsilon = 8\%$ using three different scaling parameters. We see clearly the smoothing or regularizing effect of γ: increasing γ reduces the influence of noise while blurring the contours.

In another experiment we study how the reconstructions are affected by a wrong common offset in the inversion procedure, that is, a wrong α in computing the kernel $\psi_{\mathbf{p},\gamma,3}$ (9). If we choose the common offset α_{recon} for the reconstruction larger than α_{data}, the common offset for recording the data, then the reconstructed singularities appear closer to the surface than the real singularities (top of Figure 10). The reason is that the travel time t for a given point $\mathbf{p}$ increases with the common offset. In other words: the diameter of an ellipse passing through $\mathbf{p}$ increases with the distance of the foci. This effect is more pronounced at singularities located closer to the surface because for large t and fixed foci the corresponding ellipse approximates a circle with radius $t/2$, see Figure 1. Accordingly, if $\alpha_{\text{recon}} < \alpha_{\text{data}}$ then the reconstructed singularities appear farther down than the real singularities (bottom of Figure 10).

We emphasize that singularities are displaced only in vertical direction. Their horizontal position is not affected which can be seen at the horizontal line singularity which is cleanly moved up and down, respectively.

Remark about other acquisition geometries. Other important scanning arrangements are the common midpoint (CM) and the common source (CS) geometries.

- In CM, source and receiver positions are parameterized by $s \geq 0$ as $(x_{\text{mp}} - s, 0)$ and $(x_{\text{mp}} + s, 0)$, respectively, where $(x_{\text{mp}}, 0) \in \mathbb{R}^2$ is the (fixed) common midpoint, see Figure 11.
- In CS, the source is fixed, say at $(x_{\text{sc}}, 0) \in \mathbb{R}^2$, and the receivers are located at $(x_{\text{sc}} + s, 0)$ for $s \in \mathbb{R}$, see Figure 12.

Both geometries can be handled by our approach as we will demonstrate in this remark. If a single-shot experiment[1] is performed these geometries are known to allow only the reconstruction of a very restricted set of singularities, even if full data would be available. This fact can be rigorously understood by microlocal analysis which describes how Fourier integral operators and their adjoints map singularities [20]. Using this technique, Felea et al. [12] showed that the CM geometry in radar might even introduce singularities which are not present in the original image.

With the help of Figures 11 and 12 we can easily explain a fundamental difference of CM and CS when n is layered, i.e., only depends on x_2. Recall that singularities are visible in the data only when there is an ellipse being integrated over which is tangent to

[1]Data in a seismic survey are usually recorded as a collection of common source experiments.

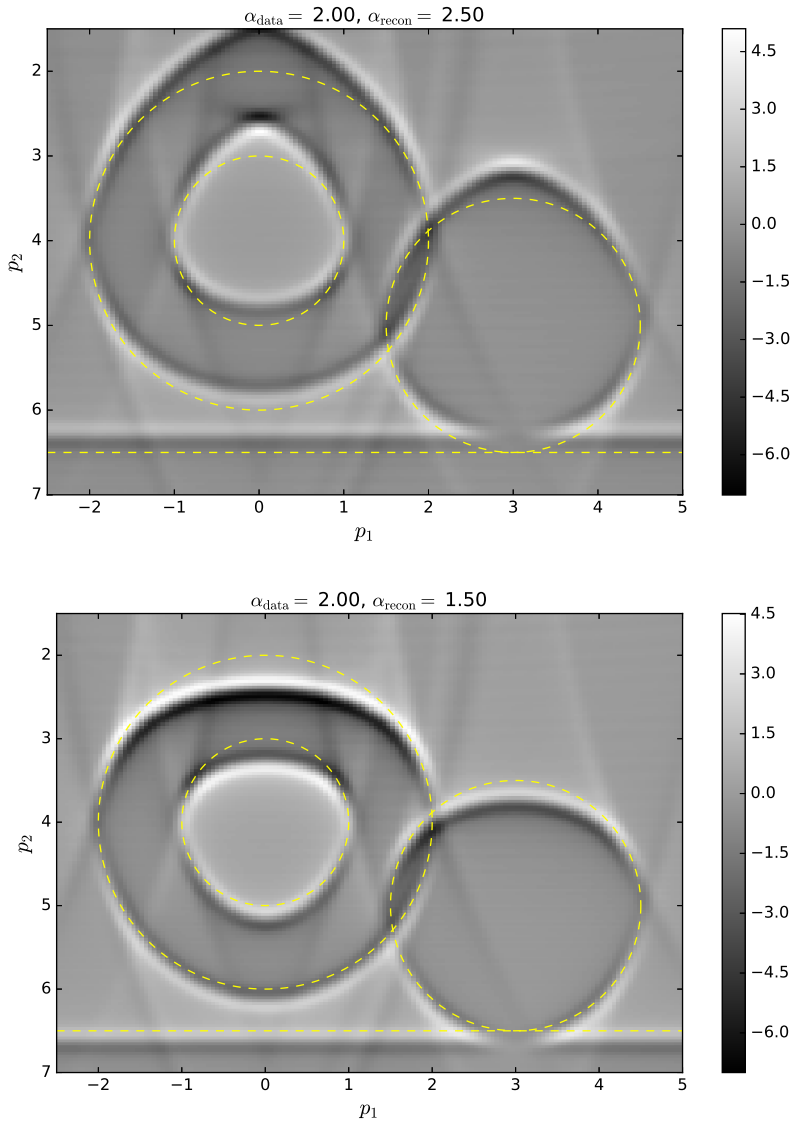

FIGURE 10. Reconstructions with a wrong common offset α_{recon} in the reconstruction kernel. The data g is generated with $\alpha_{\text{data}} = 2$ (see top of Figure 6 for the 'correct' reconstruction where $\alpha_{\text{data}} = \alpha_{\text{recon}}$). Top: $\alpha_{\text{recon}} = 2.5$, bottom: $\alpha_{\text{recon}} = 1.5$. The dashed lines indicate the singular support of n and are not part of the reconstruction.

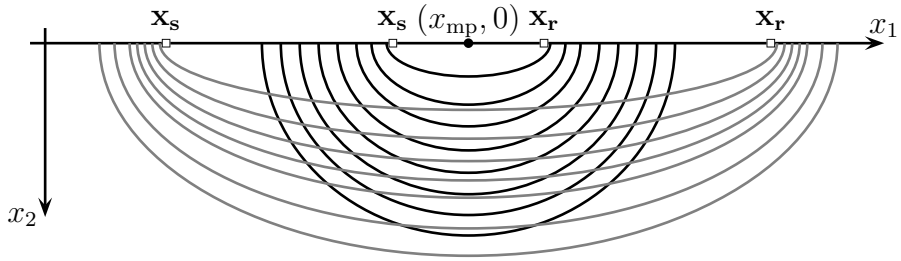

FIGURE 11. Common mid point scanning geometry.

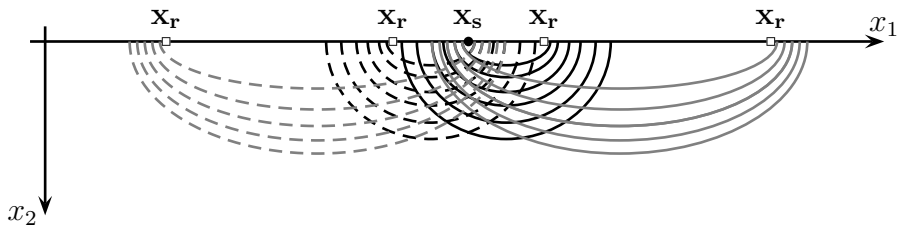

FIGURE 12. Common source scanning geometry.

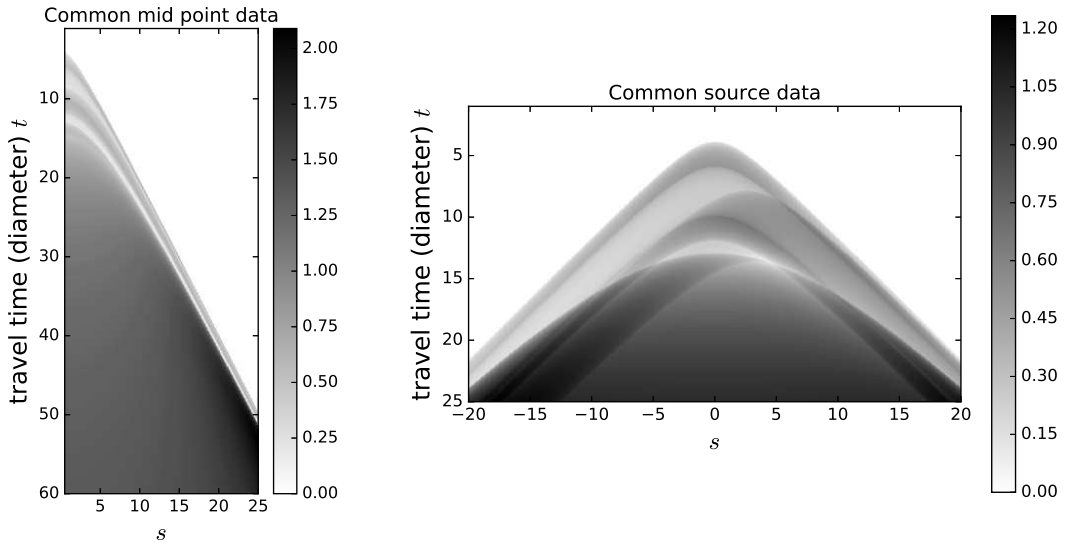

FIGURE 13. Transforms $F^{\mathrm{CM}}n$ (left) and $F^{\mathrm{CS}}n$ (right) for n from (17) where $x_{\mathrm{mp}} = 0$ and $x_{\mathrm{sc}} = 0$, respectively.

the singularity. Therefore the distribution of ellipses allows CS to detect a horizontal line singularity completely while CM only detects one point of this line located at $x_1 = x_{\mathrm{mp}}$.

Next we will highlight the shortcomings of CM and CS by numerical experiments. Our numerical scheme for the common offset geometry can easily be adapted to CM and CS based on the following relations

$$F^{\mathrm{CM}}n(s,t) = F_s n(x_{\mathrm{mp}}, t),\ s \geq 0,\ t > 2s,$$

$$F^{\mathrm{CS}}n(s,t) = F_{|s/2|}n(x_{\mathrm{sc}} + s/2, t),\ s \in \mathbb{R},\ t > |s|,$$

where F_α denotes the common offset transform (8) with offset α and F^{CM} and F^{CS} are the corresponding transforms with the CM and CS parameterizations of ellipses, respectively.

Reconstructions from the CM and CS data displayed in Figure 13 can be examined in Figure 14. We emphasize that both reconstructions would not exhibit more singularities of n if the ranges of t and s would be increased. The number of used elliptic means in each case is $N_s N_t = 600^2$, cf. (15), and $\gamma = 0.2$. Thus, the reconstructions of Figure 14 are directly comparable to the reconstructions of Figure 6.

Data from the wave equation. In the experiments so far we used data g which are in the range of the elliptic Radon transform. Now we perform experiments where the discrete data g used in (16) are generated by solving the acoustic wave equation numerically, that

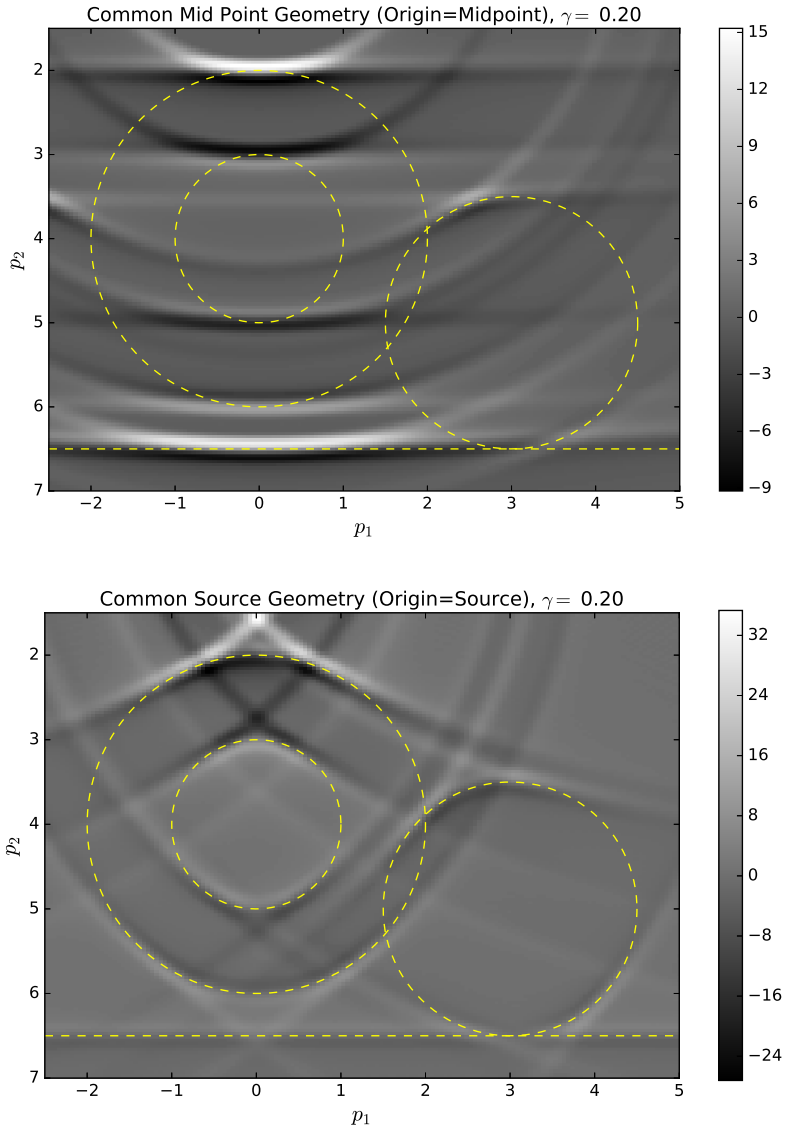

FIGURE 14. Reconstructions of n (17) from the CM (top) and CS (bottom) data which are displayed in Figure 13. The dashed lines indicate the singular support of n and are not part of the reconstruction.

is, g is an approximation to y in (6). Thus, we are a bit closer to the real situation of seismic imaging.

For the solution of the wave equations (1) and (3) as well as for recording the receiver signals we relied on `PySIT` [10] which is an open source toolbox for seismic inversion and seismic imaging. The computational domain is the rectangle $[0.1, 1] \times [0.1, 0.8]$ furnished with absorbing boundary conditions using a perfectly matched layer (PML). It was discretized by a constant step size 0.01 in each coordinate direction resulting in a Cartesian grid $\mathcal{G}$ with 90×70 points.

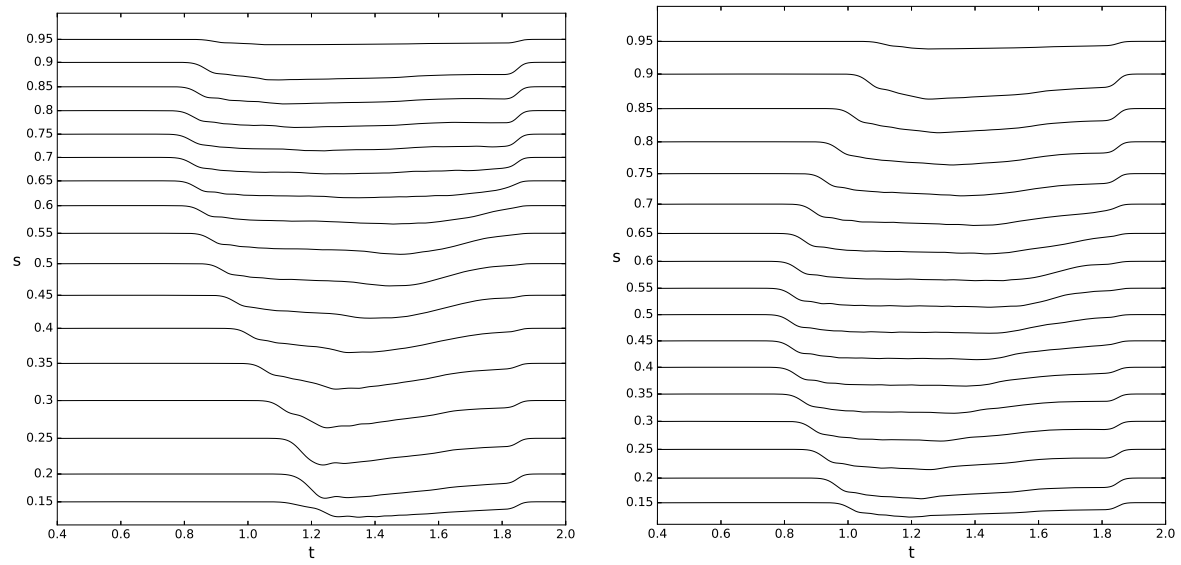

FIGURE 15. Data y of (6) as a function of time at the 17 receiver positions. The numbers at the ordinate give the midpoints s of the source/receiver pair at $(0.1, s \pm \alpha)$. Left: sine velocity profile ν_1, right: cosine velocity profile ν_2.

We considered two different sound speeds ν_1 and ν_2 each attaining exactly two different values with jumps along smooth curves:

$$\nu_1(\mathbf{x}) = \begin{cases} 1 & : \ x_2 \leq 0.1\sin(x_1) + 0.5, \\ 1.5 & : \ \text{otherwise}, \end{cases} \qquad \nu_2(\mathbf{x}) = \begin{cases} 1 & : \ x_2 \leq 0.1\cos(x_1) + 0.5, \\ 1.5 & : \ \text{otherwise}. \end{cases}$$

We used 17 source/receiver pairs with common offset $\alpha = 0.05$ positioned at $(0.1, s \pm \alpha)$, $s \in \{0.15 + 0.05i : i = 0, \ldots, 16\}$, to record the corresponding solutions u of (1) at the receivers. The (temporal) Dirac impulse modeling the source signal was approximated by a scaled (and truncated) Gaussian and the reference solution $\widetilde{u}$ of (3) was computed with constant sound speed $c = 1$. Thus, the right hand side y of (6) was available, see Figure 15.

In Figure 16 you see $\widetilde{\Lambda}_\gamma n(\mathbf{p})$ of (16) for $\mathbf{p} \in \mathcal{G}$ and $\gamma = 0.06$ where g was replaced by the y's of Figure 15. We clearly observe again that only those singularities can be detected which are tangent to ellipses being in the data set, i.e., being integrated over. This explains clearly why we recover more singularities at the example with the sine than with the cosine profile.

In our last experiment we perturb the constant background velocity 1 using

$$c(\mathbf{x}) = 1 + \frac{x_2}{8}\left(\sin(8\pi\, x_2) + \cos(6\pi\, x_1)\right)$$

for computing the reference solution $\widetilde{u}$, i.e., for obtaining the data y of (6). Note that $\min_{\mathbf{x}\in\mathcal{G}} c(\mathbf{x}) \approx 0.83$ and $\max_{\mathbf{x}\in\mathcal{G}} c(\mathbf{x}) \approx 1.19$. See bottom of Figure 17 for an illustration of this non-constant velocity. In the top of this figure you see the reconstruction $\widetilde{\Lambda}_\gamma n$ for the sine profile ν_1 using the 'wrong' kernel, that is, the kernel belonging to $c = 1$. The artifacts already existing, see top of Figure 16, are emphasized and additional artifacts show up, for instance, in the upper left part. But all in all the reconstruction is remarkably

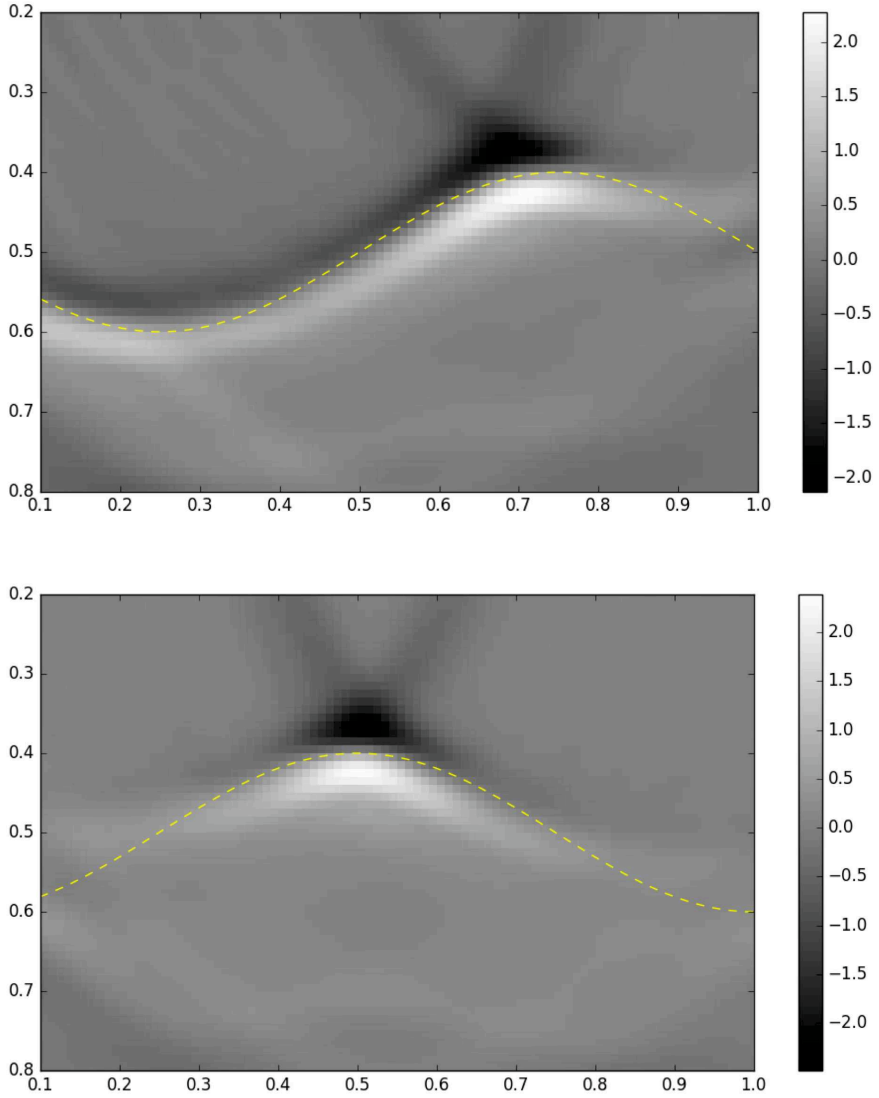

FIGURE 16. Reconstructions $\widetilde{\Lambda}_\gamma n$, $\gamma = 0.06$, from the data shown in Figure 15. Top: reconstruction from data of ν_1, bottom: reconstruction from data of ν_2. The dashed lines indicate the true singular support of ν_1 and ν_2, respectively, and are not part of the reconstructions.

stable when considering the pointwise magnitude of the relative perturbation of up to $\pm 17\%$.

Software. The `Python 2.7` code with which we have conducted the numerical experiments for the common offset geometry (Figure 6 to Figure 10) can be downloaded from `http://www.waves.kit.edu/downloads/CRC1173_Preprint_2016-37_supplement.zip`. We made use of the intrinsic parallel structure of the approximate inverse and organized the evaluation of $\widetilde{\Lambda}_\gamma n$ at different reconstruction points in parallel using the `ProcessPoolExecutor` interface provided by the `concurrent.futures` module.

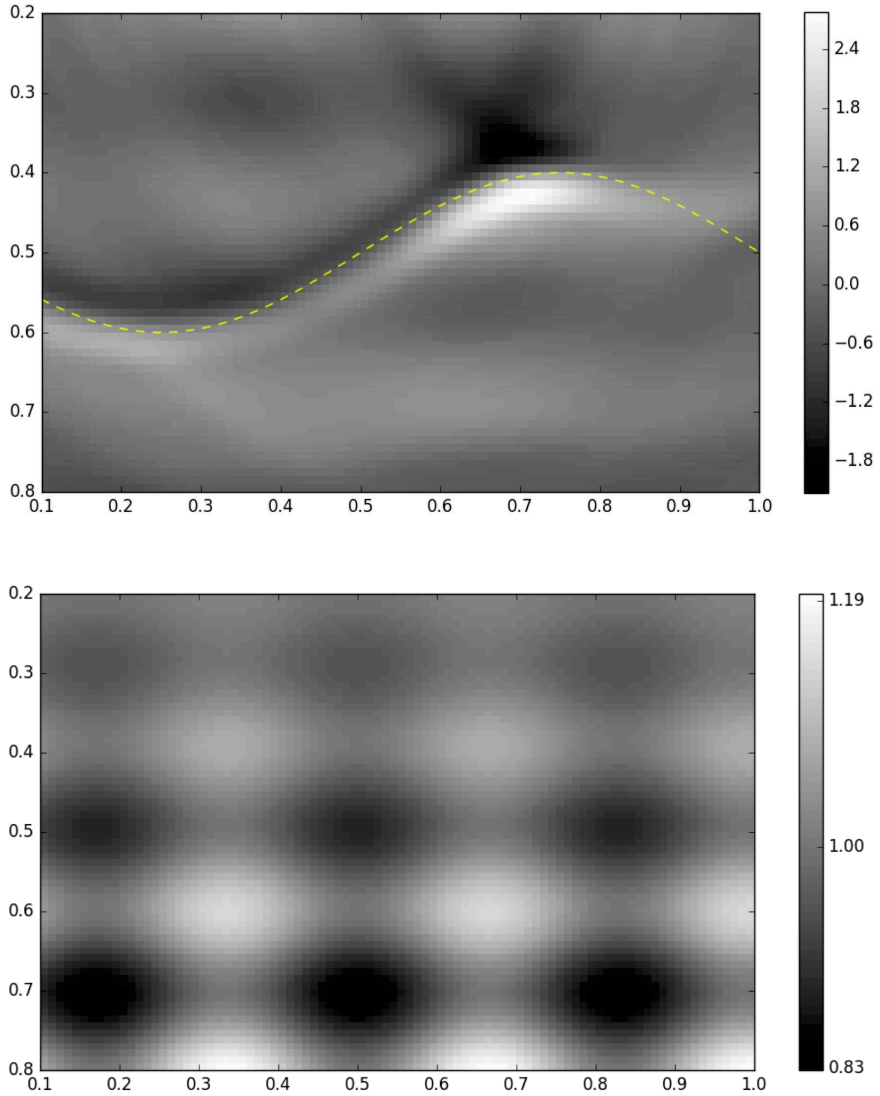

FIGURE 17. Reconstruction $\widetilde{\Lambda}_\gamma n$, $\gamma = 0.06$, with data from ν_1 (top) using a perturbed background velocity model (bottom) for computing the reference solution $\widetilde{u}$. The dashed line indicates the true singular support of ν_1 and is not part of the reconstruction.

Acknowledgments. We thank our colleague Johannes Ernesti of KIT for supporting our Python coding.

Further, we are indebted to both anonymous referees. Their meaningful comments on a previous version of this paper helped us to improve the presentation of our results.

APPENDIX A. WEIGHT CALCULATION

In this section we show how the integral

$$\widetilde{F}w(s,t) := \int w(\mathbf{x})\delta\big(t - \varphi(s,\mathbf{x})\big)\mathrm{d}\mathbf{x}$$

has to be evaluated where δ is the one-dimensional Dirac-distribution. Indeed, we will see that $\widetilde{F}w(s,t)$ has to be understood as

$$\widetilde{F}w(s,t) = \int_0^\pi w\big(\mathbf{x}(s,t,\phi)\big)\,\frac{t^2/4-\alpha^2\cos^2\phi}{\sqrt{t^2-4\alpha^2}}\,\mathrm{d}\phi \tag{19}$$

if w is integrable and supported in the lower half space. Here, $\mathbf{x}(s,t,\phi)$ are the prolate spheroidal coordinates from (10). Note that $\widetilde{F}(A\,n) = Fn$, see (8).

Our starting point is the limit representation of the one-dimensional Dirac distribution, that is,

$$\widetilde{F}w(s,t) = \lim_{h\searrow 0}\frac{1}{h}\int_{\{\mathbf{x}\in\mathbb{R}^2\,:\,t\le\varphi(s,\mathbf{x})\le t+h\}} w(\mathbf{x})\,\mathrm{d}\mathbf{x}. \tag{20}$$

Next, we express the integral using the prolate spheroidal coordinates (with t replaced by τ). The Jacobian determinant of the corresponding coordinate transform is easily calculated to be

$$\det\begin{pmatrix} \frac{1}{2}\cos\phi & -\frac{\tau}{2}\sin\phi \\ \frac{\tau/2}{\sqrt{\tau^2-4\alpha^2}}\sin\phi & \frac{\sqrt{\tau^2-4\alpha^2}}{2}\cos\phi \end{pmatrix} = \frac{\tau^2/4-\alpha^2\cos^2\phi}{\sqrt{\tau^2-4\alpha^2}}$$

which is positive because $\tau > 2\alpha$.

Applying this transformation and relying on $\varphi(s,\mathbf{x}(s,\tau,\phi)) = \tau$ we arrive at

$$\begin{aligned}\widetilde{F}w(s,t) &= \lim_{h\searrow 0}\frac{1}{h}\int_{\{\mathbf{x}\in\mathbb{R}^d\,:\,t\le\varphi(s,\mathbf{x})\le t+h\}} w(\mathbf{x})\,\mathrm{d}\mathbf{x} \\ &= \lim_{h\searrow 0}\frac{1}{h}\int_t^{t+h}\int_0^\pi w(\mathbf{x}(s,\tau,\phi))\,\frac{\tau^2/4-\alpha^2\cos^2\phi}{\sqrt{\tau^2-4\alpha^2}}\,\mathrm{d}\phi\,\mathrm{d}\tau\end{aligned}$$

which immediately implies (19) by the Lebesgue differentiation theorem.

References

[1] F. Andersson, M. V. de Hoop, and H. Wendt. Multiscale reverse-time-migration-type imaging using the dyadic parabolic decomposition of phase space. *SIAM J. Imaging Sci.*, 8(4):2383–2411, 2015.

[2] G. Beylkin. The inversion problem and applications of the generalized Radon transform. *Comm. Pure Appl. Math.*, 37(5):579–599, 1984.

[3] G. Beylkin. Imaging of discontinuities in the inverse scattering problem by inversion of a causal generalized Radon transform. *J. Math. Phys.*, 26(1):99–108, 1985.

[4] N. Bleistein, J. K. Cohen, and J. W. Stockwell, Jr. *Mathematics of multidimensional seismic imaging, migration, and inversion*, volume 13 of *Interdisciplinary Applied Mathematics*. Springer-Verlag, New York, 2001. Geophysics and Planetary Sciences.

[5] J. K. Cohen and N. Bleistein. Velocity inversion procedure for acoustic waves. *Geophysics*, 44(6):1077–1085, 1979.

[6] D. Colton and R. Kress. *Inverse acoustic and electromagnetic scattering theory*, volume 93 of *Applied Mathematical Sciences*. Springer, New York, third edition, 2013.

[7] R. Courant and D. Hilbert. *Methods of mathematical physics. Vol. II.* Wiley Classics Library. John Wiley & Sons Inc., New York, 1989. Partial differential equations, Reprint of the 1962 original, A Wiley-Interscience Publication.

[8] M. V. de Hoop. Microlocal analysis of seismic inverse scattering. In *Inside out: inverse problems and applications*, volume 47 of *Math. Sci. Res. Inst. Publ.*, pages 219–296. Cambridge Univ. Press, Cambridge, 2003.

[9] M. V. de Hoop, H. Smith, G. Uhlmann, and R.D. van der Hilst. Seismic imaging with the generalized Radon transform: A curvelet transform perspective. *Inverse Problems*, 25(2):025005, 21, 2009.
[10] L. Demanet and R. J. Hewett. `PySIT` – Seismic Imaging Toolbox for Python. `http://pysit.org`.
[11] A. Faridani, E. Ritman, and K. Smith. Local tomography. *SIAM J. Appl. Math.*, 52(2):459–484, 1193–1198, 1992.
[12] R. Felea, V. P. Krishnan, C. J. Nolan, and E. T. Quinto. Common midpoint versus common offset acquisition geometry in seismic imaging. *Inverse Probl. Imaging*, 10(1):87–102, 2016.
[13] F. G. Friedlander. *Sound pulses*. Cambridge University Press, New York, 1958.
[14] J. Frikel and E. T. Quinto. Characterization and reduction of artifacts in limited angle tomography. *Inverse Problems*, 29(12):125007, 21, 2013.
[15] J. Frikel and E. T. Quinto. Artifacts in incomplete data tomography with applications to photoacoustic tomography and sonar. *SIAM J. Appl. Math.*, 75(2):703–725, 2015.
[16] I. M. Gel′fand and G. E. Shilov. *Generalized functions. Vol. 1*. Academic Press [Harcourt Brace Jovanovich, Publishers], New York-London, 1964 [1977]. Properties and operations, Translated from the Russian by Eugene Saletan.
[17] D.l Gerth, B. N. Hahn, and R. Ramlau. The method of the approximate inverse for atmospheric tomography. *Inverse Problems*, 31(6):065002, 26, 2015.
[18] V. Guillemin and S. Sternberg. *Geometric asymptotics*. American Mathematical Society, Providence, R.I., 1977. Mathematical Surveys, No. 14.
[19] M. Haltmeier, T. Schuster, and O. Scherzer. Filtered backprojection for thermoacoustic computed tomography in spherical geometry. *Math. Methods Appl. Sci.*, 28(16):1919–1937, 2005.
[20] L. Hörmander. Fourier integral operators. I. *Acta Math.*, 127(1-2):79–183, 1971.
[21] A. I. Katsevich. Local tomography for the limited-angle problem. *J. Math. Anal. Appl.*, 213(1):160–182, 1997.
[22] V. P. Krishnan, H. Levinson, and E. T. Quinto. Microlocal analysis of elliptical Radon transforms with foci on a line. In I. Sabadini and D. Struppa, editors, *The Mathematical Legacy of Leon Ehrenpreis, 1930-2010*, volume 16 of *Springer Proceedings in Mathematics*, pages 163–182. Springer, 2012.
[23] A. Lakhal and A. K. Louis. Locating radiating sources for Maxwell's equations using the approximate inverse. *Inverse Problems*, 24(4):045020, 18, 2008.
[24] A. K. Louis. Corrigendum: "Approximate inverse for linear and some nonlinear problems" [Inverse Problems **11** (1995), no. 6, 1211–1223]. *Inverse Problems*, 12(2):175–190, 1996.
[25] A. K. Louis, M. Riplinger, M. Spiess, and E. Spodarev. Inversion algorithms for the spherical Radon and cosine transform. *Inverse Problems*, 27(3):035015, 25, 2011.
[26] D. Mitrea. *Distributions, partial differential equations, and harmonic analysis*. Universitext. Springer, New York, 2013.
[27] L. V. Nguyen. How strong are streak artifacts in limited angle computed tomography? *Inverse Problems*, 31(5):055003, 2015.
[28] B. E. Petersen. *Introduction to the Fourier transform & pseudodifferential operators*, volume 19 of *Monographs and Studies in Mathematics*. Pitman (Advanced Publishing Program), Boston, MA, 1983.
[29] E. T. Quinto, A. Rieder, and Th. Schuster. Local inversion of the sonar transform regularized by the approximate inverse. *Inverse Problems*, 27(3):035006, 18, 2011.
[30] A. Rieder, R. Dietz, and Th. Schuster. Approximate inverse meets local tomography. *Math. Methods Appl. Sci.*, 23(15):1373–1387, 2000.
[31] A. Rieder and Th. Schuster. The approximate inverse in action II: Convergence and stability. *Math. Comp.*, 72(243):1399–1415 (electronic), 2003.
[32] A. Rieder and Th. Schuster. The approximate inverse in action. III. 3D-Doppler tomography. *Numer. Math.*, 97(2):353–378, 2004.
[33] Th. Schuster. *The method of approximate inverse: theory and applications*, volume 1906 of *Lecture Notes in Mathematics*. Springer, Berlin, 2007.
[34] C. C. Stolk. Microlocal analysis of a seismic linearized inverse problem. *Wave Motion*, 32:267–290, 2000.

[35] W. W. Symes. Mathematics of reflection seismology. Technical report, The Rice Inversion Project, Rice University, Houston, TX, USA, 1998. http://www.trip.caam.rice.edu/downloads/preamble.pdf.
[36] W. W. Symes. The seismic reflection inverse problem. *Inverse Problems*, 25(12):123008, 39, 2009.
[37] M. Tygel, J. Schleicher, P. Hubral, and L. T. Santos. 2.5-D true-amplitude Kirchhoff migration to zero offset in laterally inhomogeneous media. *Geophysics*, 63(2):557–573, 1998.

Department of Mathematics, Karlsruhe Institute of Technology (KIT), D-76128 Karlsruhe, Germany
E-mail address: christine.grathwohl@kit.edu
E-mail address: peer.kunstmann@kit.edu
E-mail address: andreas.rieder@kit.edu

Department of Mathematics, Tufts University, Medford, MA 02155, USA
E-mail address: todd.quinto@tufts.edu